Evaluation and Comparison of Deep UVIS PSFs Observed at Three Epochs

L. Dressel
June 26, 2013

ABSTRACT

PSFs have been observed to a radius of 6 arcsec in filter F275W in five locations on the WFC3/UVIS detector (near the center and the four corners) at three epochs, starting during SMOV and spanning 2.3 years, to check the stability of the optics. Measurements of the PSFs have been analyzed in conjunction with the modeled breathing (departure from best focus) at the time of the exposures. The PSF encircled energy and azimuthal average have been stable beyond r ~0.25 arcsec. At smaller radii, differences in these and other modeled parameters may be due to differences in focus, which on average became more negative with time, and to undersampling of the core of the PSF by the UVIS pixels. For the PSFs near the A amplifier (upper left corner of the detector), astigmatism is apparent in the elongation of the PSF images and the modeled ellipticity. Serial CTI trails can be seen in the most recent deep exposures.

1. Introduction

Deep saturated images of a star, accompanied by less saturated and unsaturated images, were made during SMOV to assess the wings of the PSF (point spread function) at 5 locations on the WFC3/UVIS detector (WFC3 ISR 2009-38). To check the stability of the optics, we have repeated the observations made with filter F275W seven months later and 2.3 years later. Measurements in the passband of this filter are of particular interest since OTA mirror zonal polishing errors transfer the greatest fraction of flux from the PSF core into the wings at UV wavelengths and are least well modeled at the corresponding spatial frequencies. The data from all three epochs have been reduced with

the most recent reference files and analyzed in conjunction with the modeled breathing (departure from best focus) at the time of the exposures.

2. Observations

A calibration program (11438) designed to measure the WFC3/UVIS point spread function to > 5 arcsec radius at five locations on the detector was executed from 30 July to 2 August 2009 during SMOV (WFC3 ISR 2009-38). Observations with filter F275W have been repeated twice since then, in programs 11919 (04 and 24 March 2010) and 12701 (12 and 18 November 2011), to check for changes in the PSF. The target is GD153, a moderately bright (V=13.3) isolated photometric standard DA white dwarf. The star was placed near each corner of the detector ($\sim$30 arcsec from the corner in each coordinate) and near the center of the detector ($\sim$10 arcsec above the interchip gap). At each location, a series of cr-split=2 subarray exposures was made with single exposure times of 5, 10, 25, and 100 sec. Each series was constrained to be uninterrupted to limit its timespan to about 11 minutes, and thereby limit the range of position drift of the PSF on the detector and of orbital-scale focus modulation, called breathing (WFC3 ISR 2012-14). The shortest exposure time was chosen to ensure that the image of the target was unsaturated in at least one pair of exposures. The longer exposures provide improved signal-to-noise at increasingly larger radii. Each set of subarray exposures was followed by two full array exposures of 400 seconds each to image the wings of the PSF. At each position, the full set of subarray and full array exposures can thus be combined to create a high dynamic range PSF that is well exposed in the core and has good signal-to-noise out in the wings.

3. Data Reduction

The quality of the data was initially evaluated by checking the jif files for pointing and tracking problems. The rms jitter in each coordinate (V2, V3) for each cr-split pair of exposures was generally 2 to 5 mas ($\sim$0.05 to 0.13 UVIS pixels). Only one anomalous set of exposures was found: the pair of 5 sec exposures made with the target near the B amplifier (upper right corner of the detector) during program 11919. Gyro guiding mode was being used as these beginning-of-orbit exposures were made. The result of the less accurate guiding is apparent in the positions of the PSF on the detector. The PSF moved 4.5 pixels between the first and second 5 sec exposures, and an additional 0.6 pixels between the last 5 sec exposure and the first 10 sec exposure. The pointing was stable in subsequent exposures, and it was possible to use the not quite saturated 10 sec exposures to provide the brightest pixels to the composite PSF.

The raw data in all three observing programs were recalibrated with the latest reference files to produce flt files. The DQI extensions of the flt files were then modified by flagging unsaturated pixels located just above and below saturated pixels, since charge bleeds along columns from saturated pixels. These pixels were given the DQI value cor-

responding to saturation to cause them to be treated like saturated pixels during cosmic ray rejection and during the construction of the composite PSFs. They can be seen in the PSF shown in Figure 1, extracted from a 400 sec exposure with the target near amp C in the most recent calibration program (lower left corner of ibty02weq_flt.fits[1]).

Charge transfer efficiency (CTE) has been decreasing over the on-orbit lifetime of WFC3 (WFC3 ISR 2012-09), and even serial CTI loss is evident in the more recent deeply saturated PSF exposures. Pixels on the trailing side of the serial readout of saturated pixels in the long exposures were flagged with the DQI value for saturation to avoid including them in the final composite PSF. These pixels can be seen on the right side of the longest saturated column in Figure 1, since the serial readout direction for amp C is to the left. The greatest flux trailing the single saturated column above the PSF is ∼300 electrons, or about 0.4% of the saturated flux. The saturated columns are shorter in the shorter exposures; any serial CTE losses in the subarray images are obscured by the structure and relatively greater flux of the PSF at smaller radii.

Following the modification of the DQI files, the cr-split pairs of flt images were combined using the calwf3 cosmic ray rejection routine wf3rej. The parameters controlling the rejection were adjusted to ensure that it was not overly aggressive in the very high signal-to-noise core of the PSF, but still did a good job outside the core. To minimize the effect of vibrations induced by shutter motion on the PSFs in the shortest exposures (WFC3 ISR 2009-20), only the 5 sec flt images taken with the less affected SHUTRPOS=A position were used. An extra pair of 5 sec exposures was made in program 12701 so that the alternating use of SHUTRPOS A and B would produce two flt exposures with SHUTRPOS=A to combine into a crj image. For the previous observing programs, the single SHUTRPOS=A flt exposure was used in preference to a crj image, which would necessarily have included an exposure made with SHUTRPOS=B.

One additional processing step was needed for the full frame images of the PSF near the center of the detector. This PSF straddles the boundary between the quadrants of the detector read out by amp A and amp B, and electronic cross-talk is generated when the images are read out simultaneously by the two amplifiers. The readout of bright pixels on one quadrant produces a faint negative mirror-symmetric ghost in the other quadrant. The images were corrected using software provided along with WFC3 ISR 2012-02. All of the subarray exposures were read out by a single amplifier, so no correction was needed for them.

For each location on the detector in each calibration program, the calibrated images were combined to produce a single PSF with high dynamic range. Flagged pixels in the full frame image (saturated, bled into, or affected by serial CTI) were replaced by pixels in the next-longest exposure, scaled by the relative exposure time. The procedure was repeated using successively shorter exposures until all flagged pixels had been replaced. For the PSF shown in Figure 1, for example, 379, 67, 15, and 4 pixels were replaced in the crj images with exposure times 800, 200, 50, and 20 sec, respectively. The resulting composite PSFs have effective peak pixel fluxes of 5 to 8 Me-, depending on the structure of the PSF at that location, on the focus at the time of the shortest expo-
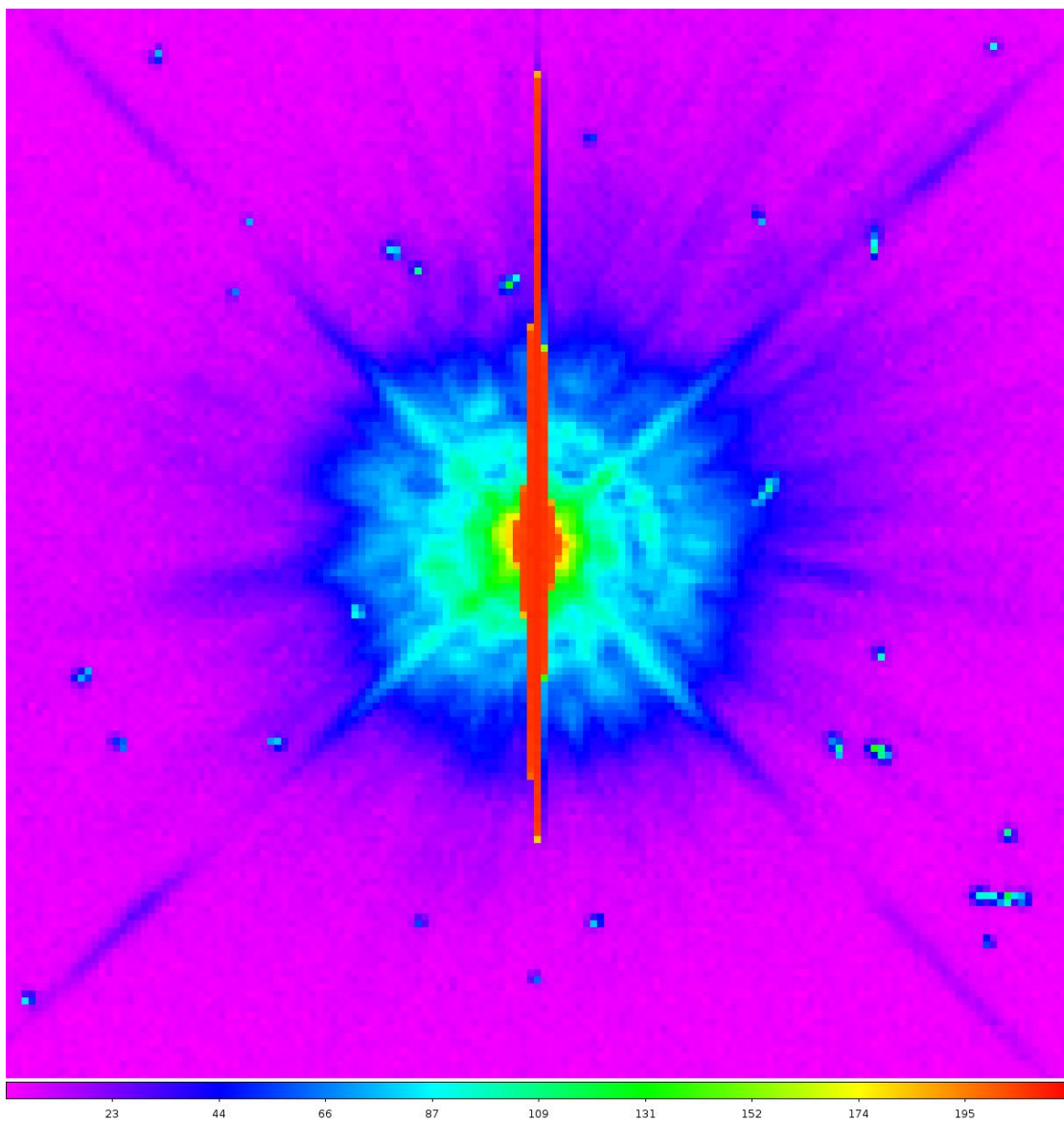
Figure 1. PSF near amp C observed in program 12701: 151x151 pixels ($\sim$6x6 arcsec) extracted from the 400 sec full frame exposure ibty02weq_flt.fits. Bleeding of flux from saturated pixels can be seen along the central columns, with trailing flux from serial CTI visible on the right side of the longest saturated column.
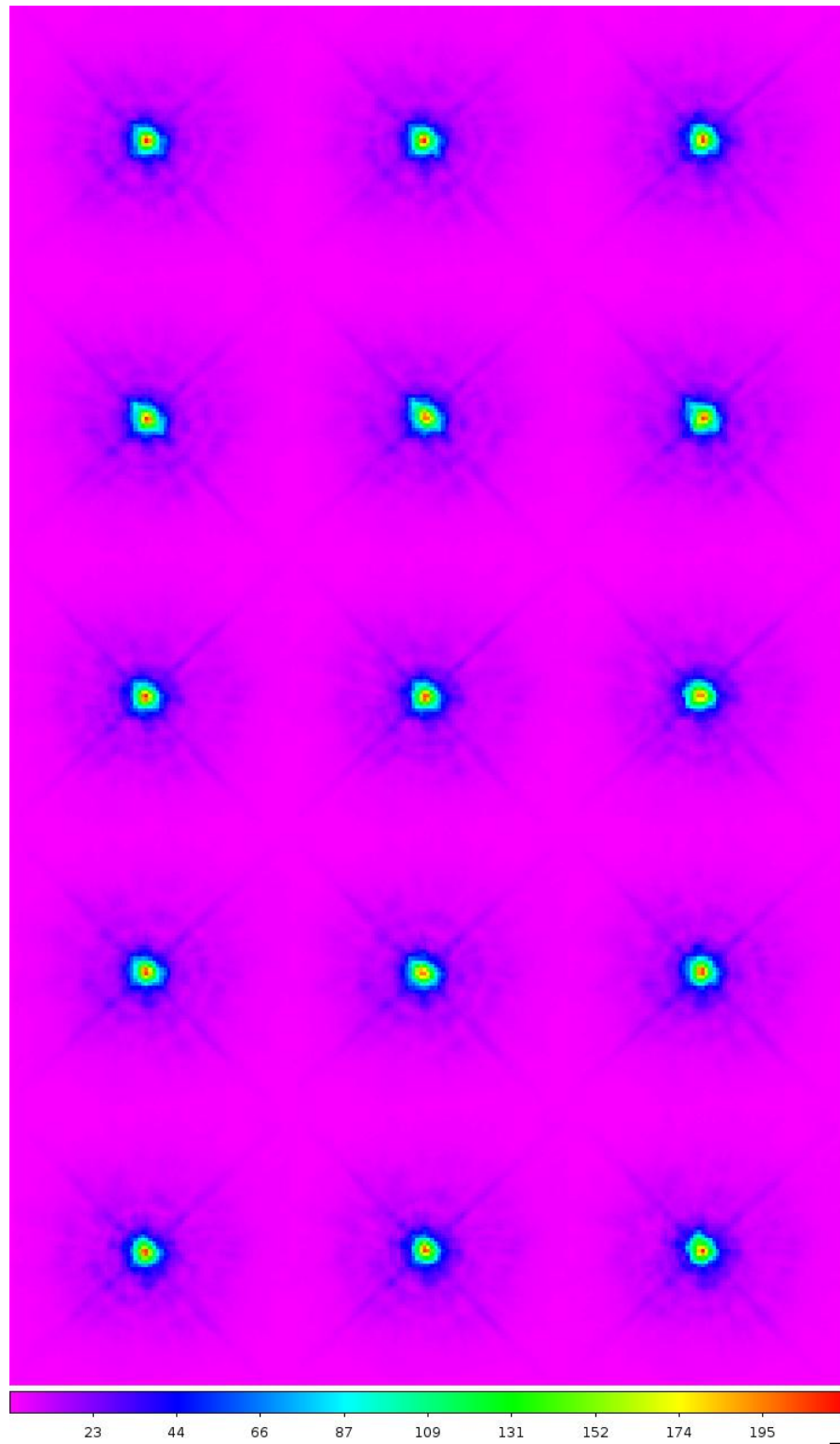
Figure 2. Montage of PSFs, 75x75 pixels each ($\sim$ 3x3 arcsec). Columns, left to right: programs 11438, 11919, 12701; rows, top to botton: positions M, A, B, C, D. The flux scale is logarithmic, with peak = log(9 Me-) for an effective exposure time of 800 sec.

sure, and on the placement of the PSF on the pixels, which undersample the core. The composite PSFs from all three observing programs (11438, 11919, and 12701) at all five positions on the detector ('M' near the middle, and near the four corners on quadrants A, B, C, and D) are displayed with a logarithmic stretch in Figure 2. Each PSF image in this montage spans 75x75 pixels, or approximately 3x3 arcmin.

4. Analysis

The composite PSFs at the five positions and three epochs have been analyzed in the same manner as the first epoch PSFs were in WFC3 ISR 2009-38. The encircled energy and azimuthally-averaged PSF were computed as a function of radius from ~1 pixel to 6 arcsec. Plots of these metrics organized by epoch are shown in Figure 3, with encircled energy as a function of radius in the left column and the azimuthal average as a function of radius in the right column. The curves computed for programs 11438 (July/August 2009), 11919 (March 2010), and 12701 (November 2011) are shown in the top, middle, and bottom panels, color coded by the position of the PSF on the detector. The same curves are plotted in Figures 4 and 5, organized by position of the PSF on the detector. Curves for PSFs near the center of the detector and near amps A and B (left and right corners of the upper chip) are shown in the top, middle, and bottom panels of Figure 4, and curves for PSFs near amps C and D (left and right corners of the lower chip) are shown in the top and bottom panels of Figure 5. In these figures, color coding indicates the observing program, and therefore the epoch of observation. Differences in the encircled energy and azimuthal average are apparent for r ≤0.2 arcsec (5 pixels). The analysis code has not been optimized to model the undersampled core in this regime.

The encircled energy of the PSFs within diameter 0.20, 0.25, 0.5, 1, 2, 4, and 6 arcsec (~5, 6.6, 12.5, 25, 50, 100, and 150 pixels) is shown in Table 1. Other measures of the PSF are shown in the remaining columns: sharpness ('shrp'), flux in the peak pixel of the normalized PSF ('peak'), FWHM in pixels, and ellipticity. The sharpness is the sum of the square of the flux in each pixel in the normalized PSF, and is therefore sensitive to the relatively high flux found in the compact core.

The encircled energy at a diameter of 2 arcsec (ee2 in Table 1, r=1 in Figures 3 through 5) and beyond is stable over the three epochs to within 0.1%. At a diameter of 1 arcsec, it is stable to 0.5%. At a diameter 0.5 arcsec, the mean encircled energy declines with time, from 0.840 to 0.838 to 0.836 for the PSFs from programs 11438 (Aug 2009), 11919 (Mar 2010), and 12701 (Nov 2011), respectively. The error in the mean is 0.001 for each epoch, so the difference between the first epoch and third epoch is formally significant at the 3 sigma level, but the sample size is small. The mean encircled energy per position appears to be lower at this diameter for the PSFs near the A amplifier than for the PSFs at the other locations, but the difference is not statistically significant for this even smaller sample size.

For metrics that are dominated by the central pixels of the PSF, more information
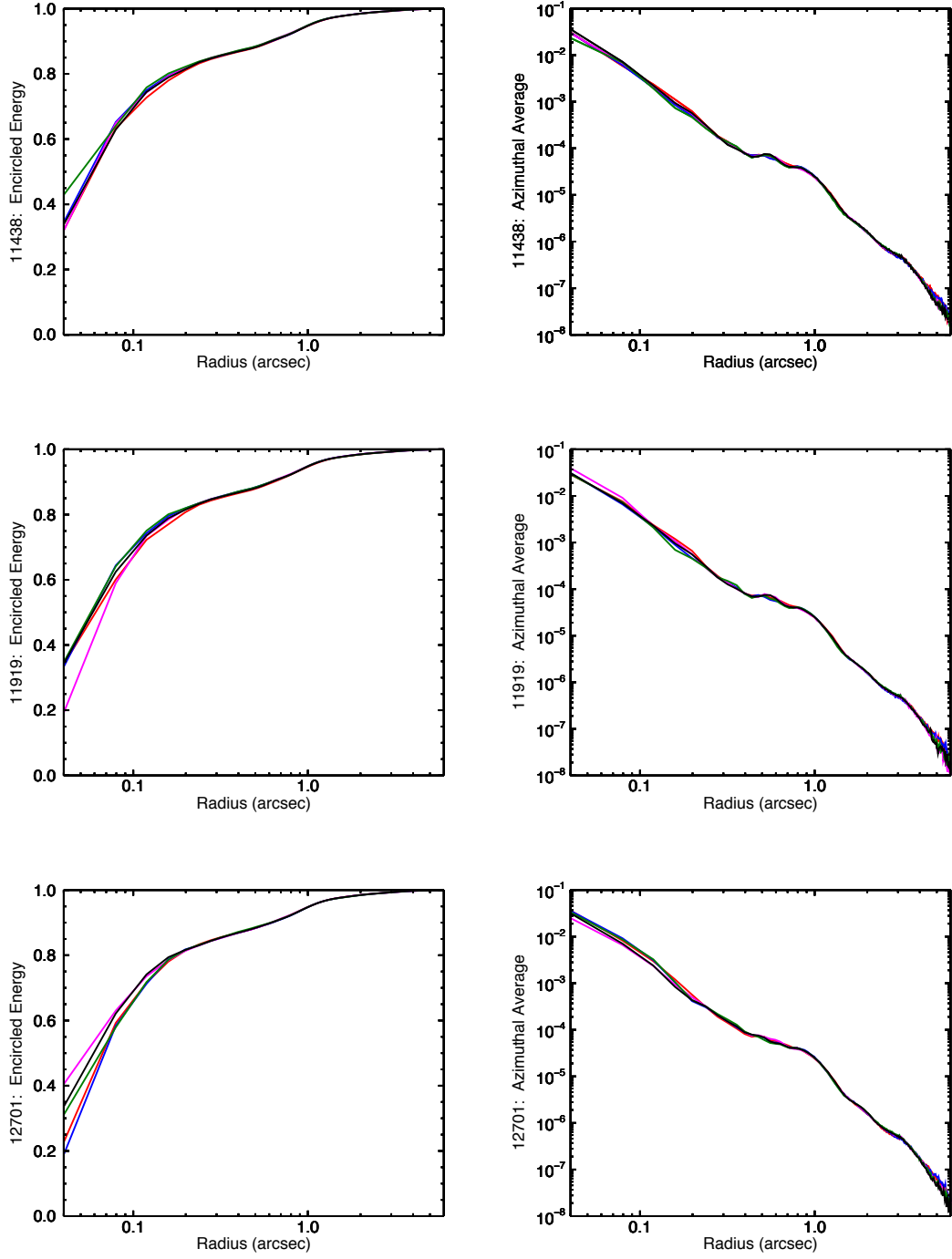
6

Figure 3. Plots of encircled energy (left column) and azimuthal average of the PSF (right column) vs radius for programs 11438 (top row), 11919 (middle row), and 12701 (bottom row). Colors indicate position on the detector: A (red), B (blue), C (magenta), D (green), M (black).
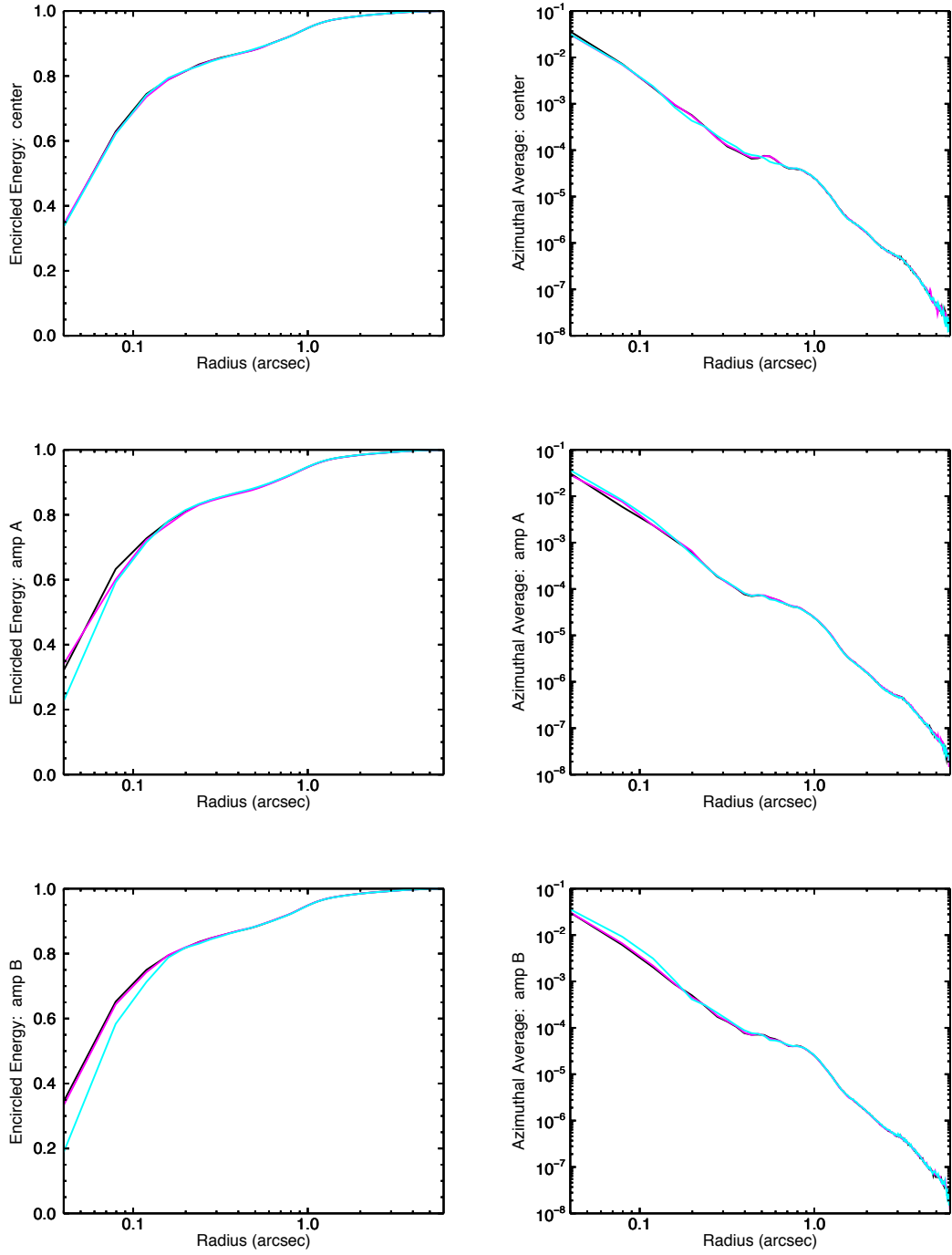
Figure 4. Plots of encircled energy (left column) and azimuthal average of the PSF (right column) vs radius for positions M (top row), A (middle row), and B (bottom row). Colors indicate observing program: 11438 (black), 11919 (magenta), 12701 (cyan).
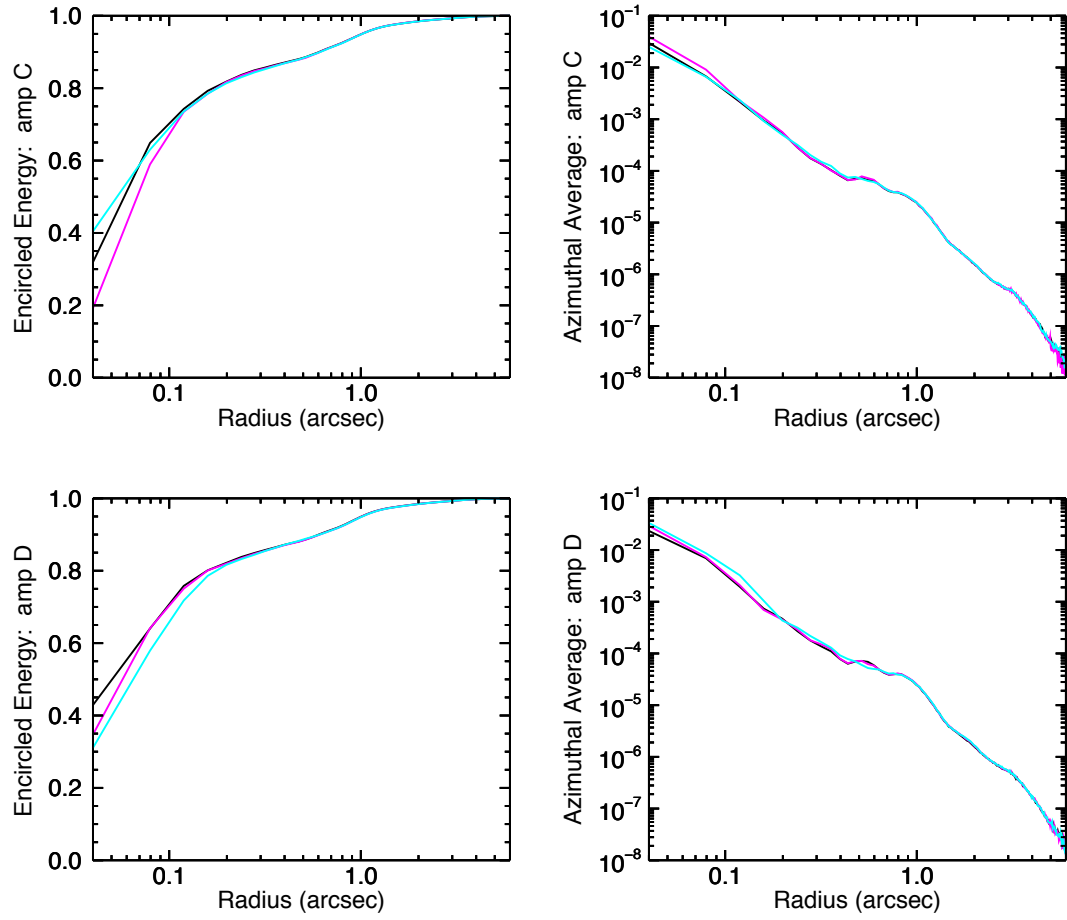
Figure 5. Plots of encircled energy (left column) and azimuthal average of the PSF (right column) vs radius for positions C (top row) and D (bottom row). Colors indicate observing program: 11438 (black), 11919 (magenta), 12701 (cyan).

Table 1. UVIS F275W PSF Measurement Summary

prop id, position	ee.20	ee.25	ee.50	ee1	ee2	ee4	ee6	shrp	peak	fwhm (pix)	ellip
11438 M	0.708	0.753	0.841	0.882	0.948	0.985	0.993	0.057	0.171	1.73	0.056
11919 M	0.696	0.747	0.838	0.881	0.948	0.985	0.993	0.055	0.161	1.74	0.036
12701 M	0.692	0.747	0.835	0.884	0.947	0.985	0.993	0.052	0.145	1.80	0.037
11438 A	0.685	0.733	0.836	0.881	0.947	0.984	0.992	0.050	0.149	1.83	0.164
11919 A	0.671	0.727	0.834	0.879	0.946	0.984	0.992	0.040	0.100	2.21	0.188
12701 A	0.675	0.732	0.838	0.883	0.948	0.985	0.993	0.044	0.126	1.99	0.006
11438 B	0.704	0.755	0.840	0.883	0.948	0.985	0.993	0.055	0.156	1.77	0.035
11919 B	0.700	0.751	0.839	0.884	0.948	0.985	0.993	0.050	0.116	1.99	0.031
12701 B	0.659	0.728	0.835	0.884	0.948	0.985	0.993	0.036	0.094	2.36	0.060
11438 C	0.701	0.752	0.841	0.884	0.949	0.985	0.993	0.051	0.138	1.90	0.083
11919 C	0.684	0.745	0.839	0.882	0.949	0.985	0.993	0.038	0.094	2.41	0.113
12701 C	0.686	0.740	0.834	0.883	0.948	0.985	0.993	0.050	0.125	1.86	0.040
11438 D	0.700	0.759	0.841	0.884	0.949	0.984	0.993	0.054	0.132	1.79	0.071
11919 D	0.705	0.759	0.839	0.884	0.948	0.984	0.993	0.052	0.139	1.87	0.081
12701 D	0.673	0.739	0.836	0.887	0.948	0.984	0.993	0.051	0.169	1.66	0.100

is needed to interpret the measurements. Because the core of the PSF is undersampled by the pixels, the distribution of flux in the central pixels is affected by the pixelation and depends on how well the PSF is centered on a pixel. Sharpness and peak pixel flux will be greater and the modeled FWHM narrower for a star well-centered on a pixel than for a star centered near the corner of a pixel. Measurements of encircled energy are increasingly dependent on the pixel centration for decreasing aperture diameter. The placement of the PSFs on the pixels to the subpixel level is therefore given in Table 2. The columns x and y give the location of each PSF in the full frame coordinate system on the relevant chip (extension 1 for the lower chip and 4 for the upper chip). The distance of the PSF ('dist') from the center of a pixel has been computed from x and y as an indication of how well centered the PSF is on a pixel. Note that the placement of the PSFs was offset during the SMOV observations relative to the later observations, because measurements of the on-orbit alignment of the WFC3/UVIS detector frame to the FGS frame had not yet been made and applied to improve the accuracy of the pointing (WFC3 ISR 2009-35).

The modeled breathing (http://www.stsci.edu/hst/observatory/focus/FocusModel) is included in the auxiliary information given in Table 2, since the PSF can be broadened and distorted by departures from best focus. Since many exposures are being combined to produce each deep PSF, large differences in breathing over the course of the exposures could affect the composite PSF. The subarray exposures and full array exposures generally spanned ~11 minutes and ~15 minutes, respectively. The average modeled breathing over the course of these exposures is given in the table in microns of dis-

Table 2. Summary of PSF Positions, Breathing, and Jitter

prop id, pos, exten	x (pix)	y (pix)	dist (pix)	Savg (μ)	Favg (μ)	Sspan (μ)	Fspan (μ)	StoF (min)	jitter (pix)
11438 M 4	2008.09	232.07	0.11	+0.7	+3.6	0.3	1.8	57.7	0.10
11919 M 4	2050.69	255.10	0.33	-2.1	+1.3	0.3	2.8	59.4	0.16
12701 M 4	2050.10	270.35	0.36	-2.1	-2.9	1.2	0.3	14.9	0.11
11438 A 4	742.15	1214.76	0.29	+2.8	+1.2	1.5	1.2	13.7	0.10
11919 A 4	802.43	1250.28	0.51	+1.9	-1.2	2.6	2.5	13.7	0.08
12701 A 4	786.32	1262.05	0.32	-1.9	+0.4	1.1	3.0	60.3	0.09
11438 B 4	3297.65	1232.74	0.44	+0.4	-0.1	0.6	0.2	13.7	0.18
11919 B 4	3345.30	1262.72	0.41	-0.7	-2.0	1.0	1.0	13.7	0.17
12701 B 4	3342.40	1273.10	0.41	-2.8	-1.6	0.5	1.8	62.5	0.10
11438 C 1	743.92	702.39	0.40	+2.2	+0.8	1.5	0.7	13.7	0.10
11919 C 1	797.40	738.05	0.40	+3.1	+0.2	2.3	2.2	13.7	0.07
12701 C 1	781.67	750.56	0.55	-0.8	-2.0	1.7	0.2	14.6	0.10
11438 D 1	3278.61	736.49	0.63	-1.1	+1.6	0.2	2.2	64.4	0.09
11919 D 1	3318.26	764.24	0.36	-1.3	-2.5	1.0	1.0	13.7	0.15
12701 D 1	3318.88	780.91	0.15	-2.9	-3.0	0.2	0.6	14.6	0.10

placement of the secondary mirror from best focus ('Savg' and 'Favg' for the subarray and full array exposures respectively). The range of focus encountered over the span of the subarray exposures ('Sspan') and the full array exposures ('Fspan') is given in the subsequent two columns. The time between the midpoint of the subarray exposures and the midpoint of the full array exposures is shown in the column 'StoF'. In some cases, the full array exposures at a given position were made in the orbit following the subarray exposures, resulting in a time separation of about an hour instead of the usual ~14 minutes. In these cases, the difference in focus ('Favg' minus 'Savg') was often relatively large and positive (~2 to 3 microns), since breathing generally exhibits a periodic curve on the timescale of an orbit with the high point near the beginning of the observing portion of the orbit. (e.g., see WFC3 ISR 2012-14.) A mismatch between the placement of the subarray PSFs and full array PSFs on a pixel could also be expected for these separated sets of exposures, since reacquisition of a target introduces an rms pointing error of ~5 to 20 mas (~0.1 to 0.5 pixels)

When the composite PSF is constructed, typically seven columns of saturated pixels in the full array exposure are replaced by pixels from the subarray exposures. (e.g., see the image of the saturated PSF in Figure 1.) These seven columns span 0.28 arcsec, so the average breathing over the course of the subarray exposures ('Savg' in Table 2) is relevant to the encircled energy within an aperture diameter of 0.25 arcsec ('ee.25' in Table 1). Six of the encircled energies at a diameter of 0.25 arcsec stand out as having the lowest values, ≤ 0.74. The A amp PSFs at all three epochs are in this set, and all but one of the third epoch PSFs are in it. Astigmatism can account for

the low encircled energies in the PSFs near A amp (ISR 2013-11). It is apparent in the diagonal elongation of the A amp PSFs in Figure 2 and in some of the ellipticities in Table 1. Poorer focus due to the long-term drift of focus to more negative values may account for the lower encircled energies in the third epoch. From the first to the third epoch, the mean focus of the subarray exposures changed from +1.0 to -2.1 microns. Although the errors in the focus model are large (rms ∼1.6 microns) due to a difficult-to-predict offset that underlies the periodic breathing structure, this change in mean focus is consistent with the gradual focus drift thought to be due to the ever more slowly proceeding desorption of moisture from the OTA truss. To compensate for this drift, the secondary mirror was moved away from the primary mirror by 3.6 microns on 24 January 2013. This was the first mirror move since the one that was made during SMOV (20 July 2009) shortly before the first epoch deep PSF observations. (See http://www.stsci.edu/hst/observatory/focus/mirrormoves.html)

The rms jitter is given in the last column in Table 2, since excessive jitter or shifts in pointing during an exposure can smear or distort the PSF. The listed value is the median of the rms jitter (quadratic sum of V2_RMS, V3_RMS) of the flt exposures used to make each composite PSF. It ranged from 0.07 to 0.18 pixels (∼3 to 7 mas). It was clearly not the dominant effect in broadening the PSFs, since it tended to be somewhat smaller for the sets of data with the broadest PSFs: the PSFs near the A amp (mean jitter 0.09 pixels) and the PSFs observed at the third epoch (mean jitter 0.10 pixels).

5. Conclusions

PSFs have been observed to a radius of 6 arcsec in filter F275W in five locations on the WFC3/UVIS detector (near the center and the four corners) at three epochs, starting during SMOV and spanning 2.3 years. The encircled energy and azimuthal average have been stable beyond r ∼0.25 arcsec. At smaller radii, differences in these and other modeled parameters may be due to differences in focus and to undersampling of the core of the PSF by the UVIS pixels. For the PSFs near the A amplifier (upper left corner of the detector), astigmatism is apparent in the elongation of the PSF images and the modeled ellipticity.

5. Acknowledgments

References

Dressel, L. 2012, "Breathing, Position Drift, and PSF Variations on the UVIS Detector", STScI ISR WFC3 2012-14

Dressel, L., Cox, C., and Lallo, M. 2009, "WFC3 SMOV Proposal 11442: Alignment of the WFC3/UVIS Apertures to the FGS Coordinate Frame", STScI ISR WFC3 2009-35

Hartig, G.F. 2009, "WFC3 SMOV Programs 11436/8: UVIS On-orbit PSF Evaluation", STScI ISR WFC3 2009-38

Noeske, N. et al. 2012, "WFC3 UVIS Charge Transfer Efficiency October 2009 to October 2011", STScI ISR WFC3 2012-09

Sabbi, E. 2009, "WFC3 SMOV Program 11798: UVIS PSF Core Modulation", STScI ISR WFC3 2009-20

Sabbi, E. and Bellini, A. 2013, "UVIS PSF Spatial & Temporal Variations", STScI ISR WFC3 2013-11

Suchov, A. and Baggett, S. 2012, "WFC3/UVIS Crosstalk Correction", STScI ISR WFC3 2012-02